

# Multi-Segment Continuum Robot Shape Estimation Using Passive Cable Displacement

William S. Rone

Robotics and Mechatronics Lab  
Department of Mechanical and Aerospace Engineering  
The George Washington University  
Washington, DC, USA  
[wsrone@gwu.edu](mailto:wsrone@gwu.edu)

Pinhas Ben-Tzvi

Robotics and Mechatronics Lab  
Department of Mechanical and Aerospace Engineering  
The George Washington University  
Washington, DC, USA  
[bentzvi@gwu.edu](mailto:bentzvi@gwu.edu)

**Abstract**—This paper describes a state estimation model for a multi-segment continuum robot that utilizes the displacement of passive cables embedded along the robot's length to estimate its overall shape. As continuum robots are used in activities outside a laboratory environment, methods of measuring their shape configuration in real-time will be necessary to ensure robust closed-loop control. However, because these robots deform along their entire length and lack discrete joints at which primary displacements take place, conventional approaches to sensing joint displacement (e.g., encoders) are inappropriate. Furthermore, elasticity plays a key role in determining the resulting shape of the continuum robot, instead of the mechanics-independent kinematic configuration frequently seen in rigid-link robotics. In order to enable accurate estimates of a continuum robot's shape, the measured displacements of passive cables are utilized to detect the change in shape of the continuum robot. An optimization is used with a static model based on the principle of virtual power to map these cable displacements into the resulting continuum robot configuration. This state estimation model was implemented numerically in MATLAB and validated on an experimental test platform.

**Keywords**—Continuum robotics, principle of virtual power, state estimation

## I. INTRODUCTION

A critical challenge facing continuum robots is shape estimation for closed-loop control. Unlike conventional robotic systems with discrete joints, continuum robots exhibit deformation along their entire length. While these robots exhibit a wide variety of benefits, from their high inherent compliance to intrinsic whole-arm manipulation to high shape flexibility when navigating crowded environments, instead of being defined by a finite set of joint angles and displacements, these robots are more accurately defined as spatial curves.

The authors' previous work has focused on modeling the mechanics of these robots by bridging the gap between the two dominant approaches of either low-fidelity lumped parameter models [1] in which each segment is treated as a circular arc, or high-fidelity distributed parameter models, in which the continuum robot is treated as a one-dimensional parameterized curve in space [2,3]. The resulting mechanics model that bridges this gap assumed a robotic structure of a serial chain of subsegment arcs within a single segment, allowing for

variations in curvature along a single segment (not possible in the low-fidelity lumped parameter model) while preserving a finite set of kinematic parameters to define the robot's shape (instead of the continuous high-fidelity distributed parameter model). The principle of virtual power was utilized to derive the mechanics, enabling modeling of the time-varying dynamics and the time-invariant statics in a single formulation. The proposed shape estimation model utilizes this mechanics model to ensure the accurate estimation of the robot's shape.

This research is motivated by future applications' need for continuum robots capable of more precise position control along the length. This is particularly true in autonomous and semi-autonomous operations in which direct teleoperation of the continuum robot is limited and instead relies on the on-board sensing to perform a specified task. In surgery, this would ensure the surgical tool accurately tracks a pre-defined trajectory based on *a priori* analysis of medical imaging. In field robotics, this would ensure accurate shape conformation of a continuum tail to actively balance a legged robot or a continuum arm grasping an object.

Previous research into continuum robot sensing has focused on shape estimation using either external sensing or integrated sensing. External sensing utilizes separate instrumentation from the robot itself, such as cameras [4,5] or ultrasound during surgery [6]. While these external sensors provide the greatest flexibility in terms of accurately measuring the robot's shape, it is not feasible for implementation outside of laboratory or surgical environments. Furthermore, there is a high computational cost for real-time image processing and shape estimation to run alongside the robot's control system. For integrated sensing, previous approaches have included inertial measurement units [7], magnetometers [8], Hall effect sensors [9], electromagnetic tracking [10] and actuation monitoring, including cable tensions [11], rod forces [12] and pneumatic pressures [13]. Each of the first four approaches track properties such as position or orientation at discrete locations along the continuum robot to ensure those specific points behave as predicted (i.e., the angle is fixed to approach an opening). The actuation monitoring is utilized primarily to ensure the actuation matches the desired actuation, though it may be used for alternatives to shape estimation for tasks such as force sensing [14] and contact point estimation [15] along

the robot. However, challenges have been demonstrated when using actuation monitoring to estimate the shape of a continuum robot when using a purely kinematic model [13].

The proposed shape estimation method utilizes the measurement of the displacements of passive cables embedded along the continuum robots in conjunction with a model of the continuum robot's mechanics to estimate the resulting shape of a continuum robot without direct measurement of the magnitude of the prescribed actuation forces.

### A. Outline

This paper is organized as follows: Section II provides background into the virtual power mechanics model used in the shape estimation model. Section III describes the mechanics-based shape estimation model, including the optimization-based approach to minimize the difference between the measured passive cable displacements and the estimated shape configuration's calculated cable displacements. Section IV describes the numerical implementation of the model in MATLAB, along with a variety of single- and multi-segment case studies to demonstrate the model's efficacy. Section V describes the experimental validation of the model using a cable-driven continuum robot.

## II. BACKGROUND: VIRTUAL POWER MECHANICS MODEL

As discussed in Section I, the key innovation in this model is the robot's discretization, shown in Fig. 1. Instead of considering each segment as either a single circular arc or a parameterized curve in space, each segment is discretized into a serial chain of subsegments to define the robot's shape. Each subsegment  $i$  is defined by three kinematic parameters: two orthogonal curvatures  $\beta_i$  and  $\gamma_i$ , and a torsional twist  $\varepsilon_i$ .

The principle of virtual power, also called Kane's method [16], utilizes variational calculus to calculate the mechanics of systems by minimizing the virtual power of the external forces and moments applied on the bodies composing the system. The total power of the system  $P$  in (1) is defined by the sum over the  $n$  bodies composing the system of the dot products of the net external forces  $\mathbf{F}_{i,ex}$  and linear velocities  $\mathbf{v}_i$ , and the net external moment  $\mathbf{M}_{i,ex}$  and angular velocities  $\boldsymbol{\omega}_i$ . A vector of the robot's curvatures and twist angles is the system's generalized coordinate vector  $q_k$ , and its derivative  $\dot{q}_k$  is the system's generalized velocity vector.

$$P = \sum_i (\mathbf{F}_{i,ex} \cdot \mathbf{v}_i + \mathbf{M}_{i,ex} \cdot \boldsymbol{\omega}_i) \quad (1)$$

To take the variation of  $P$ , the linear and angular velocities are defined with respect to the generalized velocities, as shown in (2), where  $\mathbf{v}_{i,k}$  and  $\boldsymbol{\omega}_{i,k}$  map the generalized velocities into the

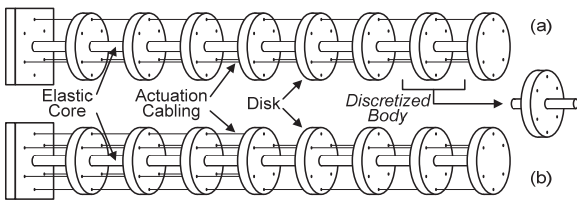


Fig. 1. Continuum robot structures utilized illustrating the disk/core discretization of the robot: (a) eight-disk, single-segment robot, (b) eight-disk, two-segment

linear and angular velocities, respectively. Substituting (2) into (1) and taking the variation results in (3). In order for the virtual power variation to equal zero (the necessary condition to minimize the virtual power), (4) must be true for any arbitrary variation in the generalized velocities  $\Delta \dot{q}_k$ .

$$\mathbf{v}_i = \mathbf{v}_{i,k} \dot{q}_k, \quad \boldsymbol{\omega}_i = \boldsymbol{\omega}_{i,k} \dot{q}_k \quad (2)$$

$$\Delta P = \left[ \sum_i (\mathbf{F}_{i,ex} \cdot \mathbf{v}_{i,k} + \mathbf{M}_{i,ex} \cdot \boldsymbol{\omega}_{i,k}) \right] \Delta \dot{q}_k \quad (3)$$

$$P = \sum_i (\mathbf{F}_{i,ex} \cdot \mathbf{v}_i + \mathbf{M}_{i,ex} \cdot \boldsymbol{\omega}_i) \quad (4)$$

The external forces and moments are defined in (5), where for each body  $i$ :  $\mathbf{F}_{i,inr}$  and  $\mathbf{M}_{i,inr}$  are the inertial forces and moments,  $\mathbf{F}_{i,act}$  and  $\mathbf{M}_{i,act}$  are the actuation transmission forces and moments due (e.g., cables or rods),  $\mathbf{F}_{i,gr}$  is the gravitational force and  $\mathbf{M}_{i,el}$  is the elastic effects (bending and torsion) moment. For static equilibrium, the inertial forces effects are omitted, and any velocity dependent terms are set to zero.

$$\begin{aligned} \mathbf{F}_{i,ex} &= \mathbf{F}_{i,inr} + \mathbf{F}_{i,act} + \mathbf{F}_{i,gr}, \\ \mathbf{M}_{i,ex} &= \mathbf{M}_{i,inr} + \mathbf{M}_{i,act} + \mathbf{M}_{i,el} \end{aligned} \quad (5)$$

The inertial effects are calculated from the kinematics of the continuum robot by determining the linear and angular positions, velocities and accelerations of each disk. Then, the inertial effects are calculated using (6), where  $m_i$  and  $\mathbf{I}_i$  are the mass and inertia tensor of body  $i$ , and  $\mathbf{a}_i$  and  $\boldsymbol{\alpha}_i$  are the linear and angular accelerations of body  $i$ .

$$\mathbf{F}_{i,inr} = -m_i \mathbf{a}_i, \quad \mathbf{M}_{i,inr} = -\mathbf{I}_i \boldsymbol{\alpha}_i - \boldsymbol{\omega}_i \times \mathbf{I}_i \boldsymbol{\omega}_i \quad (6)$$

Actuation effects are dependent on the actuation utilized. For cables, the tension of the final cable subsegment is applied at the point where the cable is tied off. On the intermediate disks, cable tensions for the surrounding cables are applied, with these forces reformulated as equivalent forces and moments on the center of mass. For actuation rods, the rod's axial force is applied directly where the rod attaches to its terminal disk. The intermediate contact forces are found by calculating the instantaneous equilibrium of the rod. In each case, friction may also be included in the calculation of these forces: the friction reduces the axial force along the actuation transmission, reducing the magnitude at the terminal disk, and adds an additional tangential force applied on each intermediate disk that is reformulated into an equivalent force and moment at the center of mass. The elastic moments (bending and torsional) due to the deformation of the continuum robot's core and actuation rods (if present) are calculated for each subsegment, and applied to the two rigid bodies adjacent to that subsegment. The bending moments are proportional to the subsegment curvatures, and the torsional moments are proportional to the twist angle. The gravitational force on each body is due to the mass of each discretized body.

More in-depth analysis of the derivation of the continuum robot mechanics of cable- and rod-driven systems may be found in [17–19]. For this paper, cables will be used to transmit actuation along the robot, using the mechanics model described in [17]. However, both single- and multi-segment models will be utilized, using the formulation for multi-segment continuum robots presented in [18].

### III. MECHANICS-BASED SHAPE ESTIMATION

In order to determine the estimate of the continuum robot shape based on a measured set of  $\eta$  measured passive cable displacements  $\delta_{j,meas}$ , an optimization is constructed comparing each measured displacement to the calculated cable displacements  $\delta_{j,calc}$  based on the current shape estimate's geometry. The objective function of this optimization should be based on the difference between each cable's measured and calculated displacements. As discussed in Section IV, the sum of the squares function (7) is utilized. The robot shape is represented in this optimization by the estimated cable tensions  $\mathbf{T}$ . At each iteration, the coupled algebraic equations defining the continuum robot's equilibrium model will be solved to determine  $q$ . Then, this  $q$  will be utilized to solve for  $\delta_{j,calc}$ .

$$\min_{\mathbf{T} \in \mathbb{R}^r} \sum_{j=1}^{\eta} (\delta_{j,meas} - \delta_{j,calc})^2 \quad (7)$$

Kinematic analysis is used to calculate the cable displacements. Three intermediate variables defined in (8) are used: the subsegment curvature magnitude  $k_i$ , the subsegment bending plane angle  $\varphi_i$  and the subsegment bending angle  $\theta_i$ , where  $L_0$  is the spacing between disks. As discussed in section II,  $\beta_i$  and  $\gamma_i$  are the orthogonal curvatures that partially define each subsegment. The coordinates  $\mathbf{p}_{i,lcl}$  of the frame  $i$  origin (at the center of mass) relative to frame  $i-1$  is found using (9), and the orientation  $\mathbf{R}_{i,lcl}$  of frame  $i$  relative to frame  $i-1$  is found using (10). In addition, the orientation  $\mathbf{R}_i$  of each frame relative to the global frame may be found recursively using (11).

$$k_i = \sqrt{\beta_i^2 + \gamma_i^2}, \quad \varphi_i = \text{atan2}(\gamma_i, \beta_i), \quad \theta_i = k_i L_0 \quad (8)$$

$$\mathbf{p}_{i,lcl} = \begin{bmatrix} c_{\varphi_i} (1 - c_{\theta_i}) / k_i & s_{\varphi_i} (1 - c_{\theta_i}) / k_i & s_{\theta_i} / k_i \end{bmatrix}^T \quad (9)$$

$$\mathbf{R}_{i,lcl} = \begin{bmatrix} c_{\varphi_i}^2 (c_{\theta_i} - 1) + 1 & s_{\varphi_i} c_{\varphi_i} (c_{\theta_i} - 1) & c_{\varphi_i} c_{\theta_i} \\ s_{\varphi_i} c_{\varphi_i} (c_{\theta_i} - 1) & c_{\varphi_i}^2 (1 - c_{\theta_i}) + c_{\theta_i} & s_{\varphi_i} c_{\theta_i} \\ -c_{\varphi_i} s_{\theta_i} & -s_{\varphi_i} s_{\theta_i} & s_{\theta_i} \end{bmatrix} \quad (10)$$

$$\mathbf{R}_i = \begin{cases} \mathbf{R}_{i,lcl} & i = 1 \\ \mathbf{R}_{i-1} \mathbf{R}_{i,lcl} & i > 1 \end{cases} \quad (11)$$

The passive sensing cables will route through the disks at a fixed position relative to the disk's center of mass. Figure 2 illustrates the three cable routing geometries to be utilized: three- and four-cable arrangements for single-segment analysis, and a six-cable arrangement for two-segment analysis. For

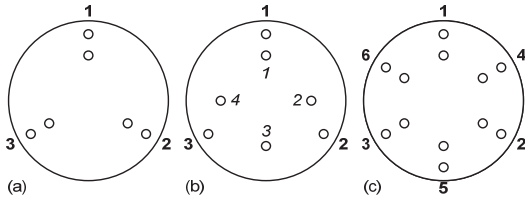


Fig. 2. Actuation (outer) and sensing (inner) cable routing holes for the three structures under consideration: (a) single-segment with three actuating and sensing cables, (b) single-segment with three actuating and four sensing cables, (c) two-segment with six actuating and sensing cables; the cables in holes labeled 1-3 terminate at disk 4.

each arrangement, a 3-by- $\eta$  matrix  $\mathbf{p}_{j,hl,sens,lcl}$  is used to define the cable sensing hole positions. As an example, the coordinates for the three-cable arrangement are defined in (12), where  $r_{hl,sens}$  is the distance of the hole from the center of mass. These local coordinates are represented in the global frame by  $\mathbf{p}_{i,j,hl,sens}$  defined in (13).

$$\kappa_j = 2\pi(j-1)/3, \quad j \in \{1, 2, 3\} \quad (12)$$

$$\mathbf{p}_{j,hl,sens,lcl} = r_{hl,sens} \begin{bmatrix} c_{\kappa_j} & s_{\kappa_j} & 0 \end{bmatrix}^T \quad (12)$$

$$\mathbf{p}_{i,j,hl,sens} = \mathbf{R}_i \mathbf{p}_{j,hl,sens,lcl} \quad (13)$$

For each cable  $j$  and subsegment  $i$ , the vector from hole  $j$  on disk  $i-1$  to hole  $j$  on disk  $i$  may be found using (14). The norm of this vector is the distance between the two holes, and the cable displacement for this subsegment is this norm subtracted from  $L_0$ . Equation (15) shows the calculation of the overall cable displacement for cable  $j$ , which terminates at disk  $\tau$ .

$$\mathbf{p}_{i,j,h2h,sens} = \begin{cases} \mathbf{p}_{i,lcl} + \mathbf{p}_{i,j,hl,sens} - \mathbf{p}_{j,hl,sens,lcl} & i = 1 \\ \mathbf{R}_i \mathbf{p}_{i,lcl} + \mathbf{p}_{i,j,hl,sens} - \mathbf{p}_{i-1,j,hl,sens} & i > 1 \end{cases} \quad (14)$$

$$\delta_{j,calc} = \tau L_0 - \sum_{i=1}^{\tau} \|\mathbf{p}_{i,j,h2h,sens}\| \quad (15)$$

### IV. NUMERICAL IMPLEMENTATION AND CASE STUDIES

#### A. Numerical Implementation

MATLAB [20] was used to implement the shape estimation model in two stages. First, an equilibrium model solver was generated in which a prescribed tension  $T$  is used to calculate the resulting generalized coordinates  $q$ . The 'fsolve' function was used to implement the model, in which the  $n$  generalized coordinates are solved using the  $n$  nonlinear equations resulting from the virtual power model. The initial guess of  $q$  in this solver is the static equilibrium configuration of the continuum robot when zero tension is applied.

Using this mechanics model, a second solver was created for the optimization posed in (7). The 'lsqnonlin' solver was used to implement the model, in which 3, 4 or 6 cable displacement difference terms are used to define the objective function. A key benefit of the 'lsqnonlin' is its separate calculation of the objective function terms. Instead of returning a single scalar value for the sum of squares, a column vector of length 3, 4 or 6 (depending on the number of sensing cables) was provided to the solver.

However, a key challenge encountered when solving this optimization arises due to the redundancy of the actuation cabling and the fact that the cabling cannot bear compressive forces. Without any modification, when solving for three input tensions for a single-segment manipulator, the optimization solver may not necessarily match the known prescribed input. For example, when a tension of 5 N is prescribed in cable 1 (or,  $\mathbf{T}_{i,input} = [5, 0, 0]^T$  N), the resulting cable displacements are found to be  $\delta_{j,calc} = [9.41, -4.43, -4.43]^T$  mm and the 'optimized' tensions are  $\mathbf{T}_{i,optim} = [5.42, 0.45, 0.45]^T$  N.

If these optimized solutions were normalized such that the lowest forces were adjusted to zero, the resulting set of tensions would be  $T_{i,shift} = [4.97, 0, 0]^T$  N. Conceptually, the challenge can be understood by imagining the continuum robot in a fully extended configuration ( $q_i = \mathbf{0}$ ) in the absence of gravity. If all three actuation cables are identically tensioned, there will be no bending or torsion, only axial deformation, in which the core contracts to generate compressive forces to oppose the actuation. Previous research [12,14,15] has used this actuation redundancy to control the compliance of the continuum robot during actuation, but in terms of shape estimation, the geometric configuration is dictated by the difference of the two cables from the cable with minimum tension. In order to minimize the robot's axial force, this will mean that at least one cable will be in zero tension for each case study. Therefore, for each segment with three actuation cables terminating in that segment, the optimization will solve for two tensions, with the third tension fixed at zero.

However, the challenge is now determining which tension to zero. Fundamentally, there are two possible approaches: (1) obtaining the information from the actuation control system, or (2) generating an algorithm for determining this from the cable displacement vector. While the first approach is simpler, it requires dedicated communication from the control system. However, greater challenges arise when trying to extrapolate the actuated cables from the cable displacements.

In order to investigate the possibility of determining cable

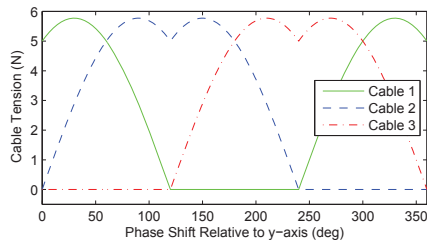


Fig. 3. Actuation tensions required to apply a constant moment loading of 0.0425 N-m to the terminal disk without friction.

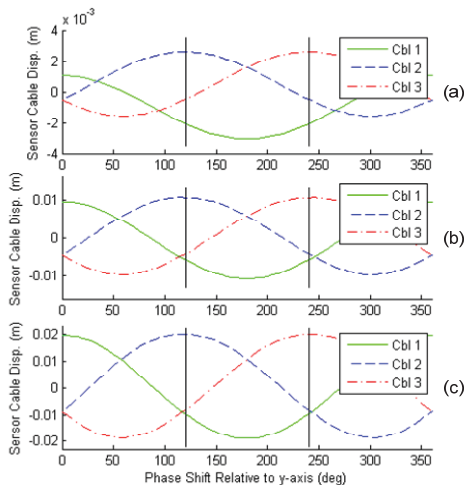


Fig. 4. Sensing cable displacement profiles corresponding to single cable tensions of (a) 1 N, (b) 5 N, (c) 10 N with vertical lines separating sectors 1 (0-120°), 2 (120-240°) and 3 (240-360°).

actuation from the measured properties, a systematic method of comparing actuation inputs is necessary. Based on the geometry of the continuum robot under consideration (discussed in Section IV-B), actuation inputs were determined to apply a uniform moment loading on the terminal disk of the robot in the absence of friction. For example, when cable 1 is actuated with a tension of 5 N, the moment loading on that terminal disk is 0.0425 N-m aligned with the y-axis. Alternatively, in order to obtain this same loading using equal actuation in cables 1 and 2, both would need to be tensioned with 5 N each, and the resulting moment would be along a vector at an angle 60° from the y-axis.

Figure 3 illustrates the required actuation of the cables ‘around’ the disk to result in a 0.0425 N-m magnitude moment in each direction. The angles along the x-axis are relative to the y-direction vector in the disk frame. The cable displacement profiles for these actuation profiles are shown in Fig. 4(b), with lines drawn at angles 120° and 240° to distinguish the three ‘sectors’ for the actuation, in which cable 3 will be zero tension (sector 1), cable 1 will be zero tension (sector 2) and cable 2 will be zero tension (sector 3). As can be seen, while the minimum cable displacement appears to be the best metric for determining the sector, there is an offset between the crossover point and the sectors themselves. Fig. 4(a,c) illustrate these same profiles for nominal cable tensions of 1 N (corresponding moments of magnitude 0.0085 N-m) and 10 N (corresponding moments of magnitude 0.085 N-m). As can be seen, the gap decreases as the bending moment increases.

Alternatively, the same analysis was performed for a four sensor cable arrangement shown in Fig. 2(b). Figure 5 illustrates the passive cable displacement profiles for this case, along with the 1 N and 10 N cases, and denotes the three sectors of the range using vertical lines. While there is greater symmetry between the four cable displacements due to their orthogonal arrangement, there is an inherent discrepancy between the cable profiles, due to the dissimilarity between the layouts. However, if a systematic algorithm could be determined to calculate the phase angle (i.e., the plot's x-coordinate) from the four values, the sector would be known.

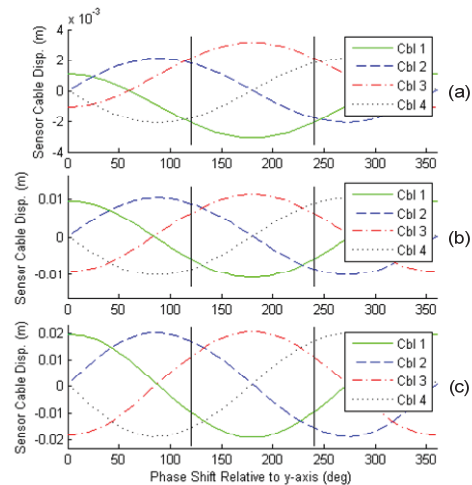


Fig. 5. Sensing cable displacement profiles corresponding to single cable tensions of (a) 1 N, (b) 5 N, (c) 10 N with vertical lines separating sectors 1 (0-120°), 2 (120-240°) and 3 (240-360°).

For the multi-segment implementation, instead of optimizing over two cable tensions, the optimization is over four cable tensions: two tensions for cables terminating in the first section and two tensions for cables terminating in the second segment. The issue of extrapolating the ‘active’ cabling from the cable displacements becomes an even larger challenge in this case, due to the loading the segment 2 cables apply on segment 1 due to their routing. As discussed in Section VI, further exploring this problem is an element of future work on this topic.

For the case studies in the following section, the properties utilized in the simulations are presented in Table 1.

### B. Case Studies

For each of the numerical case studies, a two-step process was followed: first, generate the simulated measured cable displacements; then second, utilize these values to re-calculate the original configuration/input cable tensions. For each simulation, a prescribed set of cable tensions  $T_i$  were chosen. For single segment simulations, at least one of the three tensions are set to zero, and for the multi-segment simulations, at least two are set to zero: at least one in the first three tensions (segment 1) and at least one in the second three tensions (segment 2).

For the single-segment continuum robot, two arrangements of the passive cabling were studied: a three-cable arrangement illustrated in Fig. 2(a) and a four-cable arrangement illustrated in Fig. 2(b). The three cable arrangement provides cables in the same arrangements as the actuation cables, albeit a shorter distance from the center of the disk.

For all three structures under consideration and for all actuation profiles utilized in these simulations, the optimization solver was able to successfully recalculate the original actuation to an accuracy exceeding  $1e-6$ . In the following section, the solvers are tested with realistic measured values, in which measurement error complicates the analysis.

## V. EXPERIMENTAL RESULTS

In addition to the numerical simulations utilized to test the efficacy of the mechanics-based shape estimation model, a series of experiments were also performed using a continuum robot to estimate the prescribed tensions for a system based solely on the measured passive cable displacements and knowledge of which cables are actuated.

Figure 6 shows the experimental test platform under consideration. A spring steel core (ASTM A228, 1.04 mm diameter, 240 mm long) was used with eight disks (ABS plastic, 30 mm diameter, 2 mm thick, 30mm disk spacing) mounted along the core using cyanoacrylate (Loctite 401). The

actuation and sensing cabling is PFTE-coated fiberglass thread (0.43 mm diameter). The actuation cabling was routed over spools and hanging weights were used to apply the prescribed tensions. The sensing cables were also routed over spools, and lightweight masses (0.005 N) were used to pretension the sensing cabling. The changes in heights of these masses measured using calipers (General Fractional Calipers 147) and arranged into the  $\delta_{j,meas}$  vector.

For the single-segment experiments, the measured cable displacements and estimated tension profiles are provided in Table 2 for three cases: (1) cable 1 actuated with 5 N, (2) cables 1 and 2 actuated with 5 N, and (3) cables 1 and 3 actuated with 2 N and 5 N, respectively. The maximum error using both solvers is approximately the same (10.4% for 3 cable; 10.9% for 4 cables), though the average error is less in the 4-cable sensing structure (2.89% vs. 3.98%), owing to the additional constraint in the optimization to improve accuracy.

For the multi-segment, six-cable case, the measured displacements and estimated tensions are provided in Table 3 for three cases: (1) cable 2 actuated with 5 N, (2) cable 6 actuated with 5 N, and (3) cables 2 and 6 actuated with 2 N and 5 N respectively. The maximum actuated tension error was 4.94% (case 3, cable 2), and the maximum unactuated tension error was 9.55% (case 3, cable 1). For each case, the optimization was solving for variables in which the tension was known to be (because it wasn’t loaded) zero. If an optimization was constructed to only solve for the non-zero tensions, the errors of these non-actuated tensions would disappear, and the accuracy of the actuated tensions would increase.

## VI. CONCLUSIONS AND FUTURE WORK

This paper presented a novel mechanics-based approach to shape estimation using the displacement of passive cabling embedded along single- and multi-segment continuum robots. A two-stage optimization was used to accomplish this, using the estimated actuation cable tensions as an intermediate set of variables. Using a sum-of-squares objective function composed of the differences between measured and calculated cable displacements, the cable tension vector was optimized to minimize this function. To calculate the cable displacements, the virtual power model of static equilibrium was utilized.

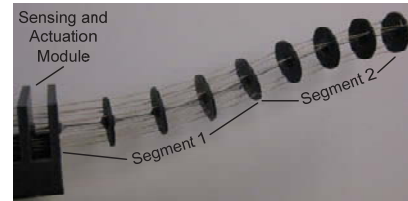


Fig. 6. Cable-driven experimental test platform set-up with two segments.

TABLE I. MATERIAL AND GEOMETRIC PROPERTIES FOR EXPERIMENTAL TEST PLATFORM.

	Property	Value		Property	Value		Property	Value
$m_i$	Disk and Subsegment Mass	$1.669 \cdot 10^{-3}$ [kg]	$I_{xx,ic1}$	Disk and Subsegment Radial Moment of Inertia	$9.821 \cdot 10^{-8}$ [kg·m <sup>2</sup> ]	$I_{zz,ic1}$	Disk and Subsegment Axial Moment of Inertia	$1.654 \cdot 10^{-7}$ [kg·m <sup>2</sup> ]
$J_{xx}$	Core Second Moment of Area	$5.743 \cdot 10^{-14}$ [m <sup>4</sup> ]	$J_{zz}$	Core Polar Moment of Area	$1.149 \cdot 10^{-13}$ [m <sup>4</sup> ]	$L_0$	Initial Subsegment Length (Disk Spacing)	30 [mm]
$E$	Core Young’s Modulus	$2.1 \cdot 10^{11}$ [Pa]	$G$	Core Shear Modulus	$8 \cdot 10^{10}$ [Pa]	$g$	Gravitational Acceleration	$9.81$ [m/s <sup>2</sup> ]
$r_{hl,act}$	Actuation Hole Radius	12.5 [mm]	$r_{hl,sens}$	Sensing Hole Radius	8.5 [mm]	$\mu$	Coefficient of Friction	0.15

TABLE II. ACTUATION ESTIMATES FOR SINGLE-SEGMENT STRUCTURES

Actuation Input (N)	3 Cbl. Disp. (mm)	4 Cbl. Disp. (mm)	3 Cbl. Actuation Estimate (N)	4 Cbl. Actuation Estimate (N)
$T_1 = 5$	9.17	9.09	5.045	4.922
	-4.48	0.54	0	0.0862
	-4.34	-8.88	0.046	0
	~	0.23	~	~
$T_1 = 5;$ $T_2 = 5$	4.32	4.60	5.055	5.032
	6.94	9.03	0	0
	-9.29	-3.92	5.372	4.896
	~	8.62	~	~
$T_1 = 2;$ $T_3 = 5$	-1.61	-1.42	1.9381	2.218
	-5.81	-8.59	0	0
	7.63	1.84	4.478	4.976
	~	8.94	~	~

TABLE III. ACTUATION ESTIMATES FOR TWO-SEGMENT STRUCTURE

Act. Input (N)	$T_2 = 5$ N					
Disp. (mm)	-3.23	5.62	-1.96	1.81	3.56	-5.21
Act. Est. (N)	-0.032	4.986	0	-0.001	0	0.236
Act. Input (N)	$T_6 = 5$ N					
Disp. (mm)	1.92	-5.11	2.96	-5.16	-3.80	10.17
Act. Est. (N)	0.226	0	-0.004	-0.021	0	5.045
Act. Input (N)	$T_2 = 2$ N; $T_6 = 5$ N					
Disp. (mm)	0.89	-2.89	1.82	-4.39	-2.82	7.97
Act. Est. (N)	0.191	1.901	0	-0.029	0	4.9081

Numerical case studies successfully recalculated prescribed cable tensions from the associated cable displacement vectors, and experimentally measured cable displacements on an experimental test platform were successfully used to estimate the configuration.

Future work will include studying methods to estimate cable tensioning from the measured displacement vector, fusing this data with alternative methods of sensing for a higher accuracy state estimate, and designing actuation/sensing modules to test the efficacy of different sensors and the utility of dual use of the actuation cables themselves for sensing. Beyond the further improvements to shape estimation, this work will also enable further improvement to the control of continuum robotic systems in applications ranging from surgery to field robotics. In surgical applications, the inclusion of passive cabling in a continuum tool, or even utilizing the measured displacement of the actuation cabling and/or rods, could supplement alternative sensing methods and fuse the data using techniques such as Kalman filtering. In field robots, compared to current alternatives, this type of sensing structure is the most feasible for integration and on-board calculation of a shape estimate to utilize in autonomous control or provide to the teleoperator while performing tasks.

#### REFERENCES

[1] R. J. Webster III and B. A. Jones, "Design and Kinematic Modeling of Constant Curvature Continuum Robots: A Review," *The International Journal of Robotics Research*, vol. 29, no. 13, pp. 1661–1683, Jun. 2010.

[2] D. C. Rucker and R. J. Webster III, "Statics and Dynamics of Continuum Robots with General Tendon Routing and External

Loading," *IEEE Transactions on Robotics*, vol. 27, no. 6, pp. 1033–1044, 2011.

[3] I. A. Gravagne, C. D. Rahn, and I. D. Walker, "Large Deflection Dynamics and Control For Planar Continuum Robots," *IEEE/ASME Transactions on Mechatronics*, vol. 8, no. 2, pp. 299–307, 2003.

[4] J. M. Croom, D. C. Rucker, J. M. Romano, and R. J. Webster III, "Visual Sensing of Continuum Robot Shape Using Self-Organizing Maps," in *IEEE International Conference on Robotics and Automation*, 2010, pp. 4591–4596.

[5] D. B. Camarillo, K. E. Loewke, C. R. Carlson, and J. K. Salisbury, "Vision Based 3-D Shape Sensing of Flexible Manipulators," in *IEEE International Conference on Robotics and Automation*, 2008, pp. 2940–2947.

[6] E. C. Burdette, D. C. Rucker, P. Prakash, C. J. Diederich, J. M. Croom, C. Clarke, P. Stolka, T. Juang, E. M. Boctor, and R. J. Webster III, "THE ACUSITT Ultrasonic Ablator: The First Steerable Needle with an Integrated Interventional Tool," *Medical Imaging 2010: Ultrasonic Imaging, Tomography, and Therapy, Proc. of SPIE*, vol. 7629, pp. 76290V–1–10, 2010.

[7] D. Rollinson, A. Buchan, and H. Choset, "Virtual Chassis for Snake Robots: Definition and Applications," *Advanced Robotics*, vol. 26, no. 17, pp. 2043–2064, Dec. 2012.

[8] J. Lee, G. Ukawa, S. Doho, Z. Lin, H. Ishii, M. Zecca, and A. Takanishi, "Non Visual Sensor Based Shape Perception Method for Gait Control of Flexible Colonoscopy Robot," in *IEEE International Conference on Robotics and Biomimetics*, 2011, pp. 577–582.

[9] P. Dario, M. C. Carozza, M. Marcacci, S. D'Attanasio, B. Magnani, O. Tonet, and G. Megali, "A Novel Mechatronic Tool for Computer-Assisted Arthroscopy," *IEEE Transactions on Information Technology in Biomedicine*, vol. 4, no. 1, pp. 15–29, 2000.

[10] R. S. Penning, J. Jung, N. J. Ferrier, and M. R. Zinn, "An Evaluation of Closed-Loop Control Options for Continuum Manipulators," in *IEEE International Conference on Robotics and Automation*, 2012.

[11] D. B. Camarillo, C. R. Carlson, and J. K. Salisbury, "Configuration Tracking for Continuum Manipulators With Coupled Tendon Drive," *IEEE Transactions on Robotics*, vol. 25, no. 4, pp. 798–808, 2009.

[12] K. Xu and N. Simaan, "Analytic Formulation for Kinematics, Statics, and Shape Restoration of Multibackbone Continuum Robots Via Elliptic Integrals," *Journal of Mechanisms and Robotics*, vol. 2, no. 1, p. 011006, 2010.

[13] W. McMahan, V. Chitrakaran, M. A. Csencsits, D. M. Dawson, I. D. Walker, B. A. Jones, M. Pritts, D. Dienno, M. Grissom, and C. D. Rahn, "Field Trials and Testing of the OctArm Continuum Manipulator," in *IEEE International Conference on Robotics and Automation*, 2006, no. May, pp. 2336–2341.

[14] K. Xu and N. Simaan, "An Investigation of the Intrinsic Force Sensing Capabilities of Continuum Robots," *IEEE Transactions on Robotics*, vol. 24, no. 3, pp. 576–587, 2008.

[15] A. Bajo and N. Simaan, "Kinematics-Based Detection and Localization of Contacts Along Multisegment Continuum Robots," *IEEE Transactions on Robotics*, vol. 28, no. 2, pp. 291–302, 2012.

[16] T. R. Kane and D. A. Levinson, "The Use of Kane's Dynamical Equations in Robotics," *The International Journal of Robotics Research*, vol. 2, no. 3, pp. 3–21, Sep. 1983.

[17] W. S. Rone and P. Ben-Tzvi, "Continuum Robot Dynamics Utilizing the Principle of Virtual Power," *IEEE Transactions on Robotics*, Accepted, 2013.

[18] W. S. Rone and P. Ben-Tzvi, "Mechanics Modeling of Multi-Segment Rod-Driven Continuum Robots," *ASME Journal of Mechanisms and Robotics*, Accepted, 2013.

[19] W. S. Rone and P. Ben-Tzvi, "Continuum Manipulator Statics Based on the Principle of Virtual Work," in *ASME International Mechanical Engineering Congress and Exposition*, 2012.

[20] MathWorks, "MATLAB and Simulink for Technical Computing," 2013. [Online]. Available: <http://www.mathworks.com/>.